A consistent record of vegetation optical depth retrieved from the AMSR-E and AMSR2 X-band observations

Mengjia Wang, Jean-Pierre Wigneron, Rui Sun, Lei Fan, Frédéric Frappart, Shengli Tao, Linna Chai, Xiaojun Li, Xiangzhuo Liu, Hongliang Ma, et al.

International Journal of Applied Earth Observations and Geoinformation 105 (2021) 102609

Contents lists available at ScienceDirect

International Journal of Applied Earth Observations and Geoinformation

journal homepage: www.elsevier.com/locate/jag

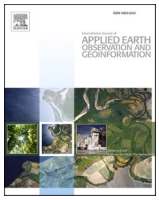

A consistent record of vegetation optical depth retrieved from the AMSR-E and AMSR2 X-band observations

Mengjia Wang [a,b,h], Jean-Pierre Wigneron [b,*], Rui Sun [a,h,*], Lei Fan [c], Frédéric Frappart [b,d], Shengli Tao [e], Linna Chai [f], Xiaojun Li [b], Xiangzhuo Liu [b], Hongliang Ma [b], Christophe Moisy [b], Philippe Ciais [g]

[a] State Key Laboratory of Remote Sensing Science, Faculty of Geographical Science, Beijing Normal University, Beijing 100875, China
[b] INRAE, UMR1391 ISPA, Université de Bordeaux, F-33140 Villenave d'Ornon, France
[c] Chongqing Jinfo Mountain Karst Ecosystem National Observation and Research Station, School of Geographical Sciences, Southwest University, Chongqing 400715, China
[d] Laboratoire d'Etudes en Géophysique et Océanographie Spatiales (LEGOS), 31400 Toulouse, French
[e] Laboratoire Evolution et Diversité Biologique, Université Paul Sabatier, Toulouse, France
[f] State Key Laboratory of Earth Surface Processes and Resource Ecology, Faculty of Geographical Science, Beijing Normal University, Beijing, China
[g] Laboratoire des Sciences du Climat et de l'Environnement, CEA/CNRS/UVSQ/Université Paris Saclay, Gif-sur-Yvette, France
[h] Beijing Engineering Research Center for Global Land Remote Sensing Products, Faculty of Geographical Science, Beijing Normal University, Beijing 100875, China

ARTICLE INFO

Keywords:
Vegetation optical depth
IB X-VOD
AGB
AMSR-E
AMSR2

ABSTRACT

Vegetation optical depth (VOD) retrieved from microwave remote sensing techniques has been used as an important proxy for monitoring the vegetation dynamics at large scales. In a first study we developed a new X-VOD indice from inversion of the X-MEB model from the Microwave Scanning Radiometer 2 (AMSR2, 2012-present) observations. The Advanced Microwave Scanning Radiometer for EOS (AMSR-E, 2002–2011) and AMSR2 share many characteristics, such as local crossing time, incidence angle, frequency at X-band, etc, which makes it possible to produce a consistent long-term X-VOD product over a long period spanning from 2002 to present. The objective of this study was to merge the AMSR-E and AMSR2 observations in order, in a second step, to produce a consistent long-term X-VOD product spanning over the combined periods of AMSR-E and AMSR2.

The main challenges in retrieving a consistent X-VOD data set from AMSR-E and AMSR2 are that (i) there is a bias between observations from the two sensors; and (ii) the lack of overlapping observations between the two sensors makes it impossible to achieve a direct inter-calibration. Here, to overcome this problem, we used AMSR-E slow rotation data (AMSR-E L1S), which has similar characteristics as AMSR-E and provided observations concurrently with AMSR2, as a bridge to calibrate the AMSR-E brightness temperature (TB) observations with AMSR2 TB.

As our main objective in this TB calibration study was to produce a consistent long-term AMSR-E/AMSR2 X-VOD product, we evaluated the retrieved X-VOD product based on different inter-calibration, either global-based or pixel-based, methods. Both AMSR-E and AMSR2 X-VOD were evaluated against the Aboveground Biomass (AGB), Leaf Area Index (LAI) and the Normalized Difference Vegetation Index (NDVI). The results suggest that global-based inter-calibration methods using homogeneous and temporally stable land covers (Evergreen Broadleaf Forests and Snow and Ice) as reference calibration data sets provided the best results. For instance, the spatial relationships between X-VOD and AGB/LAI/NDVI are highly consistent over the AMSR-E and AMSR2 periods after the calibration work. This study laid a solid foundation for monitoring the dynamics of X-VOD, as a proxy of AGB, over the combined periods of AMSR-E and AMSR2 sensors (almost 20 years).

* Corresponding authors at: INRAE, UMR1391 ISPA, Université de Bordeaux, F-33140 Villenave d'Ornon, France (J.-P. Wigneron). State Key Laboratory of Remote Sensing Science, Faculty of Geographical Science, Beijing Normal University, Beijing 100875, China (R.Sun).
E-mail addresses: jean-pierre.wigneron@inrae.fr (J.-P. Wigneron), sunrui@bnu.edu.cn (R. Sun).

https://doi.org/10.1016/j.jag.2021.102609
Received 23 July 2021; Received in revised form 27 October 2021; Accepted 28 October 2021
Available online 1 November 2021

1. Introduction

Vegetation dynamics plays an important role in the carbon-, water- and energy-cycles through regulating the carbon economy of plants, the water transformation from soil to plants and to the atmosphere by evapotranspiration, and the surface latent heat flux (Prigent et al., 2007; Duveiller et al., 2018; Wang et al., 2020; Yu et al., 2021). Vegetation optical depth (VOD), a variable used to parameterize microwave-based vegetation extinction effects, has supported these research fields by offering a proxy to study vegetation water content (Wigneron et al., 1995; Wigneron et al., 2017; Feldman et al., 2018; Tian et al., 2018), vegetation water status (Konings and Gentine, 2017) or above-ground biomass (AGB) (Liu et al., 2015; Bastos et al., 2018; Brandt et al., 2018; Fan et al., 2019; Tong et al., 2020; Wigneron et al., 2020; Qin et al., 2021). Consistent long-term VOD products are required in all the above-mentioned studies.

A wide range of space-borne sensors have been used to retrieve VOD products at global scale (Du et al., 2017; Baur et al., 2019; Frappart et al., 2020; Wigneron et al., 2021). In particular, AMSR-E and its successor AMSR2 provide daily and global multi-frequency passive microwave observations from 2002 to the present (JAXA, 2009, 2016). We concentrated on the X-band (10.65 GHz) observations in the present study, considering its deeper penetration capacity than higher frequencies (W, Ka, and K-bands) (Kolassa et al., 2016) and its lower sensitivity to Radio Frequency Interference (RFI) than lower frequencies (C-band) (de Nijs et al., 2015). VOD products have been retrieved from X-band AMSR-E and AMSR2 signals using various algorithms (Owe et al., 2001; Du et al., 2015). Recently, Wang et al. (2021) used a method based on the inversion of the X-band microwave emission of the biosphere (X-MEB) model to retrieve X-VOD (referred to as INRAE Bordeaux (IB) X-VOD) in Africa. IB X-VOD was evaluated with AGB, LAI and NDVI and it showed a very satisfactory performance in comparison to the existing X-VOD products.

Even though AMSR-E and AMSR2 sensors share many characteristics, there is still a bias between the observations from the two sensors (Wu et al., 2020). Thus, inter-calibrating the AMSR-E and AMSR2 TB observations is a pre-requisite to produce a consistent AMSR-E/AMSR2 X-VOD products. In addition, a nine-month data gap between the termination of AMSR-E and the subsequent initiation of AMSR2 (JAXA, 2009, 2016) further challenges the accuracy of inter-calibration algorithms. Therefore, the key question in producing a consistent AMSR-E/AMSR2 X-VOD data set is to define how to bridge the gap between the AMSR-E and AMSR2 observations. For example, Moesinger et al. (2020) chose the Tropical Rainfall Measuring Mission Microwave Imager (TMI) as a bridge and used cumulative distribution function to merge the X-VOD products retrieved from different sensors. Du et al. (2014), similarly, chose a third sensor, the Microwave Radiation Imager (MWRI) onboard the FengYun 3B satellite, but mainly focused on the TB inter-calibration instead of the retrieved products. However, there are some potential issues in these approaches due to the discrepancy of some characteristics between AMSR-E/AMSR2 and the sensors used to make a bridge, such as the local crossing time and the incidence angle.

In order to achieve a direct inter-calibration with the observations from its successor (AMSR2), AMSR-E was restarted with a slow rotation mode (2 rotations per minutes (rpm), hereafter called AMSR-E L1S). Hu et al. (2019) used AMSR-E L1S to calibrate K (18.7 GHz) and Ka (36.5 GHz) bands of AMSR2 TB with AMSR-E TB as the reference data and then produced a continuous record of near-surface soil freeze/thaw status. Similarly, Meier and Ivanoff (2017) modified AMSR2 TB at K- (18.7 GHz, 23.8 GHz) and Ka- (36.5 GHz) bands into equivalent AMSR-E TB with the help of AMSR-E L1S, and depicted sea ice changes over a long period. However, AMSR-E L1S has not yet been exploited widely at X-band and the current studies (Yao et al., 2021) have been limited to SM retrievals. To the best of the authors' knowledge, there is no AMSR-E L1S-based merging study investigating the consistency of retrieved X-VOD between AMSR-E and AMSR2 periods.

Considering this context and in order to produce a consistent AMSR-E/AMSR2 X-VOD data set, the main questions we addressed in this study are:

(i) to explore different calibration approaches in order to obtain consistent time series between AMSR-E and AMSR2 TB;
(ii) to compare the consistency of the calibrated AMSR-E TB and AMSR2 TB;
(iii) to retrieve X-VOD from the calibrated AMSR-E TB data using the X-MEB model and to assess the consistency of the relationship between X-VOD and AGB/LAI/NDVI spanning over the combined periods of AMSR-E and AMSR2.

2. Data and methodology

2.1. Data

2.1.1. Microwave observations

AMSR-E on board NASA Aqua satellite measured the Earth surface from June 2002 to October 2011 (https://nsidc.org/data/amsre/). Aqua had a Sun-synchronous sub-recurrent orbit, consequently leading to twice daily surface microwave observations by the AMSR-E sensor with ascending/descending orbit crossing time at 13:30/01:30 ± 15 mins local standard time, respectively. AMSR-E flied at an altitude of 705 km at an incidence angle of 55°and with a ground swath of about 1450 km. The antenna had a size of 1.6 m and a normal rotation of 40 rotations per minutes (rpm). AMSR-E provided horizontally (H) and vertically (V) polarized TB observations and the frequency of X band is 10.65 GHz (Kawanishi et al., 2003).

AMSR-E sensor stopped operating on October 4, 2011, but was restarted with a slow rotation mode of 2 rpm (AMSR-E L1S) for 3 years (December 5, 2012 to December 4, 2015, https://suzaku.eorc.jaxa.jp/GCOM_W/research/). Fig. 1 illustrates the spatial distribution of the TB observed by AMSR-E L1S and AMSR2 on the same day (August 30, 2014) and the limited number of observations made by AMSR-E L1S. The other characteristics of AMSR-E L1S, such as polarizations and frequencies, are the same as for AMSR-E (see Table 1).

The Japanese Aerospace Exploration Agency (JAXA) launched AMSR2, on the Global Change Observation Mission 1st–Water (GCOM-W1) satellite (https://suzaku.eorc.jaxa.jp/) in May 2012. As a follow-on sensor, AMSR2 shares most of the characteristics as AMSR-E, such as a sun-synchronous sub-recurrent orbit, local crossing time, incidence angle, antenna rotation frequency, swath width and polarization. Compared with AMSR-E (Aqua), the differences for AMSR2 are: a slightly lower orbit altitude of GCOM-W1 (699.6 km) and a larger antenna size (2.0 m) (Imaoka et al., 2010; Zhang et al., 2021).

The present study selected observations during night-time in consideration of the near-thermal-equilibrium circumstances of the surface soil, canopy and air as suggested by Owe et al. (2008).

2.1.2. ERA5 reanalysis dataset

The European Centre for Medium-Range Weather Forecasts (ECMWF) system releases a series of land surface reanalysis datasets (https://cds.climate.copernicus.eu/), of which ERA5 is a new generation. ERA5 provides estimates with a spatial resolution of 0.25° and a temporal resolution of one hour, and shows visible improvements compared to its predecessor ERA-Interim (Ma et al., 2021). ERA5 dataset including soil moisture (SM, 0–7 cm), skin temperature, soil temperature within 2 layers (0–7 cm and 28–100 cm) were used as input in the X-VOD retrieval from the X-MEB model. In order to keep the modelled and microwave datasets temporally consistent, we extracted ERA5 data from the closest observed time of the AMSR-E & ASMR2 observations for each pixel and each day.

2.1.3. Evaluation datasets

In order to assess the consistency of long-term X-band VOD retrieved

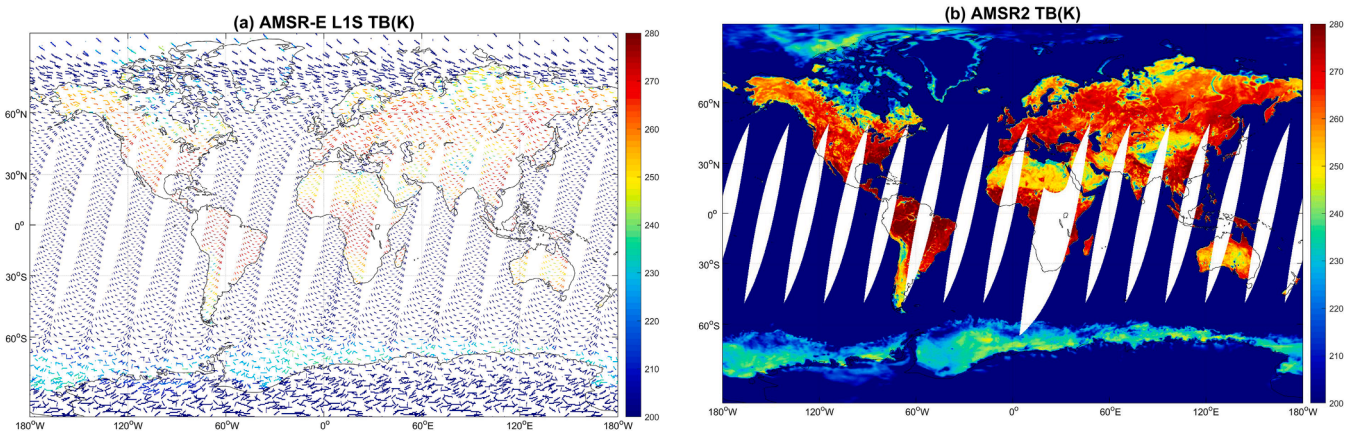

Fig. 1. Brightness Temperature at H polarization for descending orbits observed on August 30, 2014 by AMSR-E L1S (a) and AMSR2 (b).

Table 1
Characteristics of the satellites/sensors used in this study.

Specifications	AMSR-E	AMSR-E L1S	AMSR2
Satellite Platform	AQUA	AQUA	GCOM-W1
Period of Availability	June 2002 - October 2011	December 2012 - December 2015	July 2012 - present
Altitude (above the equator)	705 km	705 km	699.6 km
Antenna size	1.6 m	1.6 m	2.0 m
Footprint (scanning × proceeding)	29.4 km × 51.4 km	29.4 km × 51.4 km	24 km × 42 km
Antenna rotation	40 rpm	2 rpm	40 rpm
Frequency at X-band	10.65 GHz		
Recorded spatial resolution	0.25°		
Orbit	Sun-synchronous sub-recurrent		
Crossing time (Local standard time)	13:30/01:30 ± 15 mins for Ascending/Descending		
Incidence angle	55°		
Swath width	1450 km		
Polarizations	H and V		

from the calibrated AMSR-E TB and AMSR2 TB data sets, we selected two AGB data sets around the year 2010, Bouvet AGB and GlobBiomass AGB and two optical vegetation indices, LAI and NDVI, and we evaluated their relationships with the retrieved X-VOD from the two AMSR-E and AMSR2 sensors. To keep the evaluation datasets spatially consistent with X-VOD, Bouvet AGB (25 m), GlobBiomass AGB (100 m), LAI (1 km) and NDVI (1 km) were resampled to a spatial resolution of 0.25°. All these vegetation variables and indices are based on optical and Synthetic Aperture Radar (SAR) and inventory datasets. Therefore, the retrieved X-VOD in this study is absolutely independent of these vegetation variables.

2.1.3.1. Bouvet AGB. Bouvet AGB was produced based on the Phased Array L-band SAR observations and has an overall good accuracy considering the validation result against the field measurements (root mean squared error (RMSE) = 17 $Mg{\cdot}ha^{-1}$) (Bouvet et al., 2018). This AGB estimate only includes sparse vegetation, such as savannahs and woodlands. Conversely, Mermoz et al. (2015) produced a AGB distribution in the tropical forests. These two data sets were combined into an AGB dataset in the whole Africa (hereafter called Bouvet AGB).

2.1.3.2. GlobBiomass. The GlobBiomass project, supported by the European Space Agency (ESA), aims at increasing the knowledge on the global distribution of AGB (http://globbiomass.org/products/global-mapping). GlobBiomass was calculated by combining multiple satellite observations of SAR backscatter around the year 2010. Evaluation against measurements from field inventory plots showed that the spatial patterns and magnitude of AGB were well captured. The uncertainty of GlobBiomass AGB averaged over Africa was estimated at 23.6 % (Rozendaal et al., 2017).

2.1.3.3. LAI and NDVI. LAI and NDVI are provided by the Copernicus Global Land Service (CGLS) (https://land.copernicus.eu/global/). These two products were derived from SPOT/VGT (Satellite Pour l'Observation de la Terre - VEGETATION sensor) data since May 1998 until December 2013 and from PROBA-V (Project of on-board autonomy - VEGETATION instrument) since January 2014 onwards. As the present study focused on evaluating the consistency between the X-VOD data sets retrieved from AMSR-E and AMSR2, we did not consider the whole observation period of AMSR-E and AMSR2 but focused our study on the last running year of the AMSR-E period (September 2010 - August 2011) and the first running year of the AMSR2 period (August 2012 - July 2013). Therefore, LAI and NDVI used in this study are both based on SPOT/VGT data. Quality control was conducted according to Swinnen and Toté (2017).

2.2. Methodology

TB calibration was performed at a global scale, while the X-VOD evaluation step was achieved only over the African continent because the X-MEB model used to retrieve X-VOD in this study has only been evaluated over Africa so far (Wang et al., 2021). The African continent includes a large variety of vegetation features and climates which is sufficient to make a detailed evaluation of the consistency of the retrieved X-VOD retrieved from both AMSR-E and AMSR2.

2.2.1. Inter-calibration of the AMSR-E and AMSR2 TB observations

There is a nine-month data gap after the AMSR-E instrument stopped until AMSR2 started providing observations, thus AMSR-E L1S was used to build a bridge between the AMSR-E and AMSR2 observations. Given that i) AMSR2 has a larger antenna diameter of 2.0 m, consequently providing a better footprint resolution along scanning and proceeding directions than AMSR-E, and ii) AMSR2 has an improved component, named high temperature noise source (HTS) and used for microwave absorbing warm-end calibration, leading to a higher radiometric quality than AMSR-E (Shimoda et al., 2012), we chose AMSR2 as the reference TB data set. The approach used is a two-fold approach consisting in: i) inter-calibrating the AMSR-E L1S and the AMSR2 TB observations using AMSR2 as the reference and ii) using this inter-calibration to calibrate the AMSR-E TB observations (assuming that the AMSR-E L1S and AMSR-E TB observations have very similar characteristics).

We first pre-processed AMSR-E L1S TB by i) extracting the geometrical information for each pixel and each orbit; ii) removing data with

poor quality according to the quality information (AMSR-E L1S, 2013); iii) integrating data from all descending orbits (usually 14 orbits each day) into daily observation data. Next, we calibrated the AMSR-E (L1S) TB observations using four methods. In consideration of the sparse observations of AMSR-E L1S, global-based (Method 1 & 2) and pixel-based (Method 3 & 4) methods were tested. These four different methods are detailed below.

2.2.1.1. Method 1. Method 1 builds a global linear function, respectively for H and V polarization, between AMSR-E L1S and AMSR2 TB using all non-water pixels. To ensure data comparability, we used the AMSR2 TB observations acquired in the periods during which AMSR-E L1S TB data were also available. We used the averaged TB values over the AMSR-E L1S period (December 5, 2012 - December 4, 2015) to build the calibrated functions for the two polarizations as follows:

$$TB^{AMSR-E}_{calibrated} = \mathrm{a} \times TB^{AMSR-E}_{original} + b \quad (1)$$

where a and b represent, respectively, the slope and intercept which have to be calibrated.

Previous literature suggested time-varying regression coefficients between AMSR-E L1S and AMSR2 TB should be used (Meier and Ivanoff, 2017). Thus, in addition to calibrating using all land types (Method 1), we also tested calibrating using only temporally stable land covers (Method 2, see below) as the reference data set.

2.2.1.2. Method 2. Method 2 is similar to Method 1 except that the calibration only includes TB observations over dense forest (EBF) and surfaces covered by permanent ice and snow. The rationale of using these surfaces is that they have a lower standard deviation of TB than the other land classes (Fig. 2) and should be more stable temporally to serve as calibration targets. Choosing homogeneous and temporally stable sites to do the comparison and calibration work has also be done in previous studies (Shimada, 2011; Bhatt et al., 2014). Das et al. (2014) additionally considered desert but we excluded barren areas in this study because they presented higher standard deviations than the other selected (dense forests, ice, snow) targets. Method 2 has the advantage, compared to Method 1, of avoiding errors resulting from seasonal instability of bias between AMSR-E (L1S) and AMSR2. In addition, the large range of TB values provided by high (EBF) and low (ice and snow) TB values enables to build a robust calibration function.

2.2.1.3. Method 3 & 4. Method 3 and 4 are pixel-based methods which means that calibration functions were built (and then used) separately for each pixel. The two methods (3 & 4) consist of applying corrections so that AMSR-E (L1S) TB have the same mean ($\overline{\mathrm{TB}}$) and standard deviation values (σ(TB)) as AMSR2 TB. This method, as given in Eq. (2) and (3), has often be used to calibrate or merge two data sets (Haerter et al., 2011; Fang et al., 2015).

$$\sigma(\mathrm{TB}) = \sqrt{\frac{\sum_{i=1}^{n}(TB_i - \overline{TB})^2}{n}} \quad (2)$$

$$TB^{AMSR-E}_{calibrated} = \frac{\sigma(TB^{AMSR-2})}{\sigma(TB^{AMSR-E1S})} \times \left(TB^{AMSR-E}_{original} - \overline{TB^{AMSR-E1S}}\right) + \overline{TB^{AMSR-2}} \quad (3)$$

In consideration of the limited available observations of AMSR-E L1S due to its slow rotation mode, two different methods were tested:

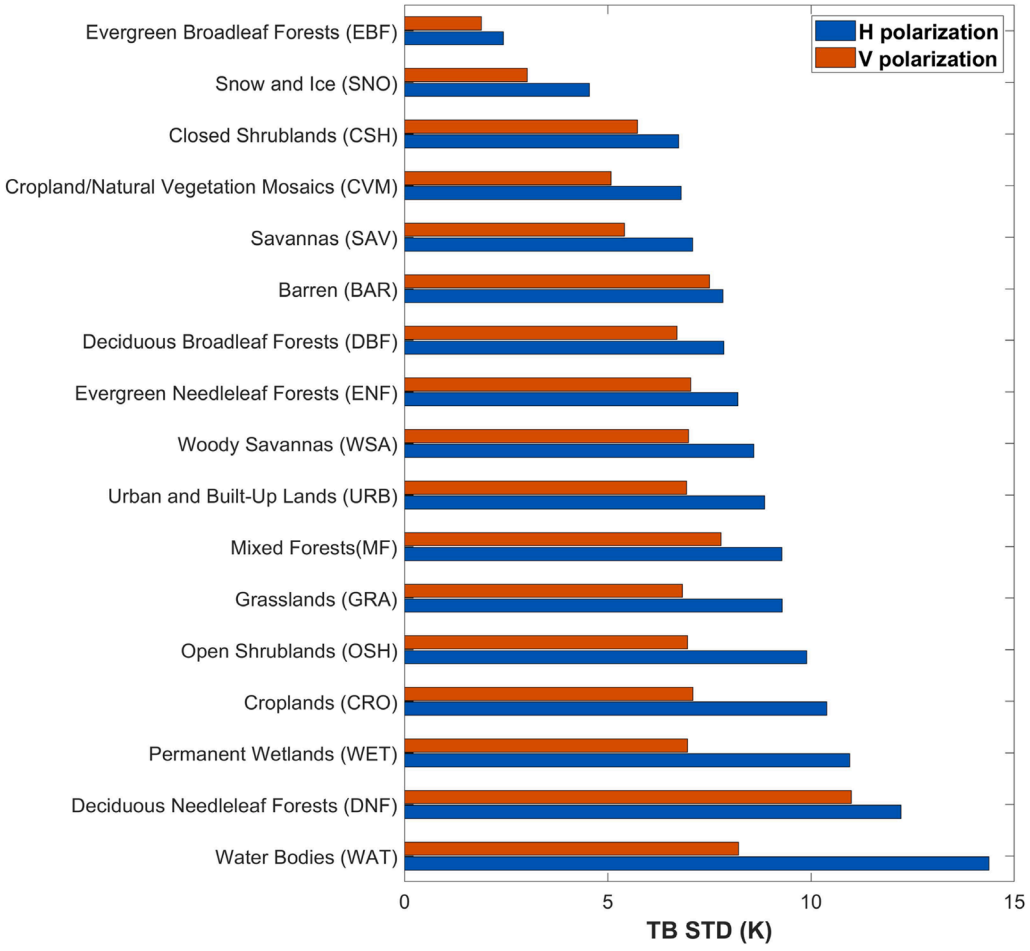

Fig. 2. Standard deviation of AMSR2 TB over the AMSR-E L1S period (December 2012 - December 2015) for each IGBP class.

Method 3: only the AMSR-E L1S & AMSR2 TB data acquired at the same dates were kept; meaning that, for a given date, the AMSR2 TB data were kept only if AMSR-E L1S is also available;

Method 4: all the available AMSR2 and AMSR-E L1S TB data over the AMSR-E L1S period were used.

All the four methods tested here are very complementary: the advantage of Method 1 & 2 is that we have a large number of training data to build a robust and reliable function, however, the function may not be perfectly suitable for all pixels. It is the opposite for methods 3 & 4: they are pixel-based methods, but for some pixels, we only have a very limited number of observations which may degrade the reliability of the calibrated functions.

2.2.2. X-MEB model

The X-MEB model is based on τ-ω model (a zero-order radiative transfer equation) (Mo et al., 1982). Wang et al. (2021) exclusively retrieve X-VOD from inversion of the X-MEB model, while the other parameters, such as SM, the effective soil temperature (T_G) and vegetation temperature (T_C) were estimated from the ancillary data. Considering the good performance of ERA5 soil moisture against in situ measurements (Beck et al., 2020; Li et al., 2020), ERA5 SM was used as the input SM data set in the X-MEB model. T_G was calculated from ERA5 soil temperatures according to Wigneron et al. (2007b) and Wigneron et al. (2008). T_C was calculated from ERA5 skin temperature. More details on the X-MEB model are given in Wang et al. (2021).

2.2.3. Evaluation of the consistency of X-VOD

Considering the reference values of VOD from in-situ measurements are not available, it is difficult to directly validate VOD at the satellite scale (Liu et al., 2011). Prior studies suggest strong links between X-VOD and AGB (Wigneron et al., 2007a; Liu et al., 2015), LAI (Kumar et al., 2020) and NDVI (Jones et al., 2012; Tian et al., 2016). Accordingly, an alternative option to assess the X-VOD performances could be to compare X-VOD with these related parameters (Rodríguez-Fernández et al., 2018; Li et al., 2021). Similarly, here we assessed the consistency of the AMSR-E and AMSR2 X-VOD products over two periods by analysing their spatial relationships with AGB/LAI/NDVI. The consistency between the AMSR-E and AMSR2 X-VOD products was evaluated using several error metrics (Eq. (10)–(14)): correlation coefficients (R), root mean squared error (RMSE), unbiased root mean square error (ubRMSE) and bias (Willmott, 1981; Chen et al., 2017).

$$R = \frac{\sum_{i=1}^{n}\left[\left(X-\overline{X}\right)\times\left(Y-\overline{Y}\right)\right]}{\sqrt{\sum_{i=1}^{n}\left(X-\overline{X}\right)^2}\sqrt{\sum_{i=1}^{n}\left(Y-\overline{Y}\right)^2}} \tag{4}$$

$$RMSE = \sqrt{\frac{1}{n}\sum_{i=1}^{n}(X-Y)^2} \tag{5}$$

$$ubRMSE = \sqrt{\frac{1}{n}\sum_{i=1}^{n}\left[\left(X-\overline{X}\right)-\left(Y-\overline{Y}\right)\right]^2} \tag{6}$$

$$Bias = \overline{(Y-X)} \tag{7}$$

where $\overline{X}$, $\overline{Y}$ and $\overline{(Y-X)}$ represent, respectively, the averaged values of X, Y and (Y-X).

We present a flowchart summarizing the different steps of the approach, including i) the inter-calibration between AMSR-E and AMSR2 TB by different methods (marked with different colors); ii) the retrieval of X-VOD; and iii) the evaluation of the retrieved X-VOD products against three vegetation variables (AGB, LAI, NDVI). During the inter-calibration step, we used both the AMSR-E L1S and AMSR2 datasets (reference data) acquired between December 5, 2012 and December 4, 2015 (the life period of AMSR-E L1S). For the two following steps (VOD retrieval and evaluation), the AMSR-E data come from the last running year of the AMSR-E period (September 1, 2010 to August 31, 2011; note that we did not use the last month of the AMSR-E observations to avoid any possible instability of the sensor just before termination) and AMSR2 data come from the first running year of the AMSR2 period (August 1, 2012 to July 31, 2013, similarly, AMSR2 observations acquired during the first month of operation were not used to avoid possible instabilities of the sensor just after launch). The Bouvet and GlobBiomass AGB maps used in this study represent AGB circa year 2010 which is close to both the selected AMSR-E and AMSR2 periods. The LAI and NDVI datasets, used to evaluate AMSR-E and AMSR2 X-VOD, come from the corresponding periods of the selected AMSR-E and AMSR2 observations.

3. Results

3.1. Comparison of the AMSR-E, AMSR-E L1S and AMSR2 TB data

3.1.1. Comparison of AMSR-E and AMSR2 TB

AMSR-E and AMSR2 TB were compared by plotting the time series of TB observations over two periods per 0.25° of latitude with each grid recorded as a longitudinally averaged TB (Hovmöller diagram, Fig. 3(a, b)). As shown in Fig. 3(a, b), both AMSR-E (June 2002 - October 2011) and AMSR2 (July 2012 - present) TB show similar spatio-temporal patterns during their respective operation periods. However, the TB observations from AMSR2 are warmer than those measured from AMSR-E for both H and V polarizations. In order to avoid perturbating effects due to surface changes, caused by vegetation growth or deforestation, etc, over the whole AMSR-E & AMSR2 period (almost 20 years), we chose the last running year of the AMSR-E acquisition period (September 1, 2010 to August 31, 2011) and the first running year of the AMSR2 acquisition period (August 1, 2012 to July 31, 2013) to evaluate the similarities and differences between the AMSR-E and AMSR2 TB observations. AMSR-E and AMSR2 TB were found to be strongly correlated as expected, with correlation coefficient (R) reaching almost 1 (0.99) for the H (V) polarization (Fig. 3 (c, e)). The average biases between AMSR2 and AMSR-E TB were 3.93 K and 3.10 K, respectively, for the H and V polarization, which is illustrated in the histogram of bias in Fig. 3 (d, f). The same analyses were conducted for homogeneous and temporally stable areas, such as EBF to further compare the two sensors (Appendix Fig. 1). Over those surfaces the bias and ubRMSE values decreased in comparison to values obtained over all land cover pixels, falling from 3.93 K to 3.11 K (H) and from 3.10 K to 2.77 K (V) for bias, and from 3.54 to 1.26 K (H) and from 3.09 to 0.70 K (V) for ubRMSE. In general, these results indicated the strong consistency between the AMSR-E and AMSR2 TB observations but also the presence of a clear bias.

3.1.2. Comparison between AMSR-E and AMSR-E L1S TB data

Considering the thermal environment around HTS may be different between 40- and 2-rpm observation modes (Imaoka et al., 2016), the AMSR-E and AMSR-E L1S TB observations were compared. As shown in Fig. 4(a, b), AMSR-E and AMSR-E L1S TB exhibit similar spatio-temporal patterns for both the H and V polarizations but with a trivial discontinuity in October 2013 due to missing data after quality control (data with poor quality were removed). To compare the yearly averaged TB from AMSR-E and AMSR-E L1S, we used high-quality AMSR-E L1S data acquired in a period from April 1, 2014 to March 31, 2015 during which TB observations were continuously recorded without data missing. As for AMSR-E, the last running year was chosen to reduce the temporal gap between the two datasets at its minimum. Fig. 4 (c, e) shows that AMSR-E and AMSR-E L1S TB are strongly correlated with R reaching 0.97 and 0.98 at H and V polarizations, respectively. The bias between AMSR-E L1S and AMSR-E TB is very close to zero with mean values of 0.47 K (H) and 0.19 K (V) for all land covers and 0.49 K (H) and 0.12 K (V) for the EBF class (Appendix Fig. 2). These results indicate a good consistency between the AMSR-E and AMSR-E L1S TB data and confirm the

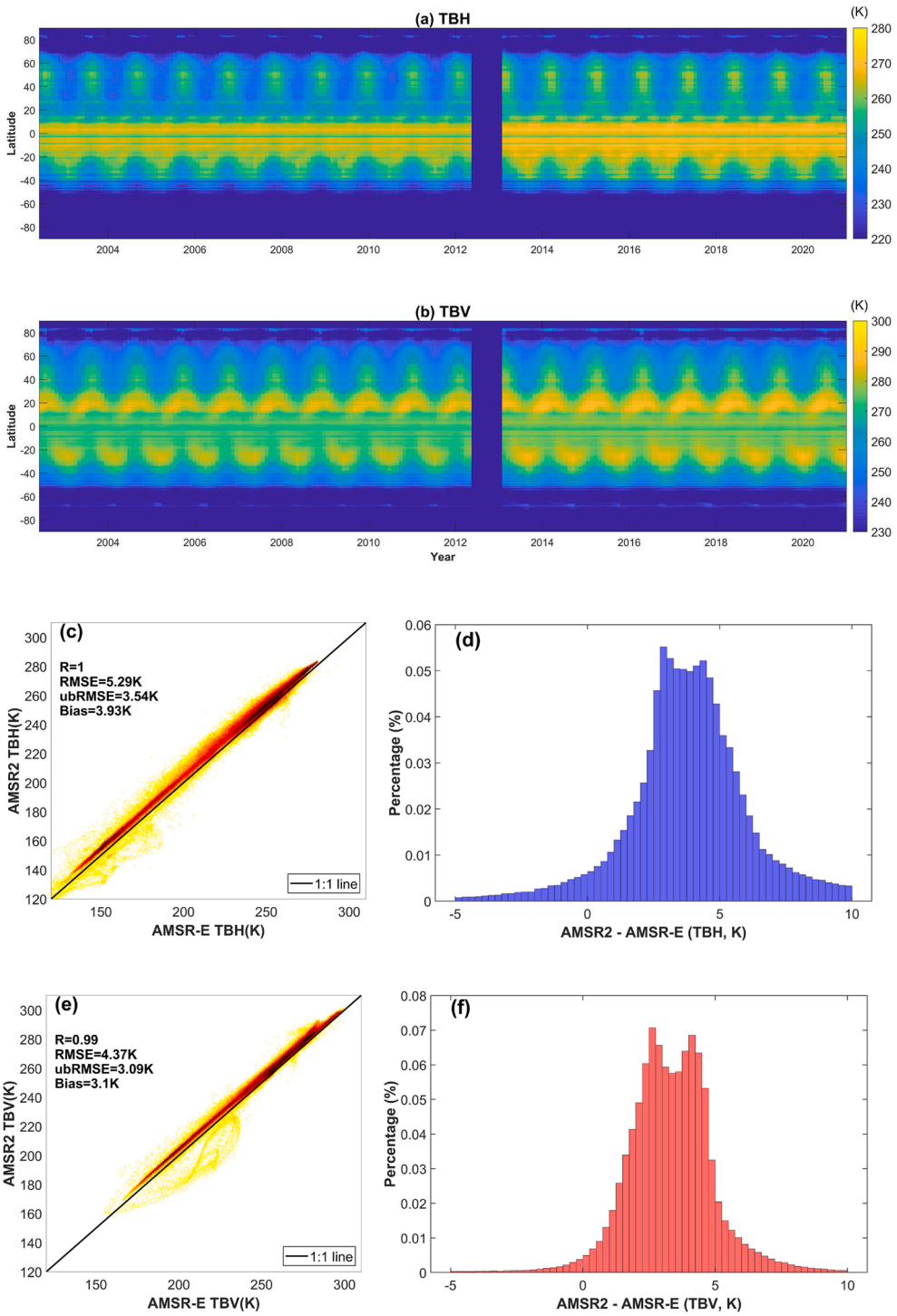

Fig. 3. Hovmöller diagrams showing the monthly mean values of TB per latitude for AMSR-E and AMSR2 TB over they respective observation periods at H (a) and V (b) polarizations; Scatter plot of AMSR-E (September 2010 to August 2011) and AMSR2 (August 2012 to July 2013) TB observations at H (c) and V (e) polarizations; Histogram of the difference between AMSR2 and AMSR-E TB observations at H (d) and V (f) polarizations.

interest of using the AMSR-E L1S TB data for our AMSR-E/ AMSR2 merging study.

3.2. Inter-calibration between AMSR-E and AMSR2

Four methods were applied to calibrate AMSR-E TB: two of them are global-based methods (Methods 1 & 2) and the two others are pixel-based methods (Methods 3 & 4). The calibrated formulas for the global-based methods are given in Table 2 and Appendix Fig. 3. The maps of slope and intercept for the pixel-based methods are showed in Fig. 5.

Four different methods were preliminarily assessed by comparing the calibrated AMSR-E TB (the last running year, from September 2010 to August 2011) and the AMSR2 TB (the first running year, from August 2012 to July 2013) (Fig. 6). There may exist some changes in surface conditions (vegetation and soil moisture) between two years, leading consequently to different TB values for a single pixel and single day. Therefore, comparisons were conducted in a global and yearly term

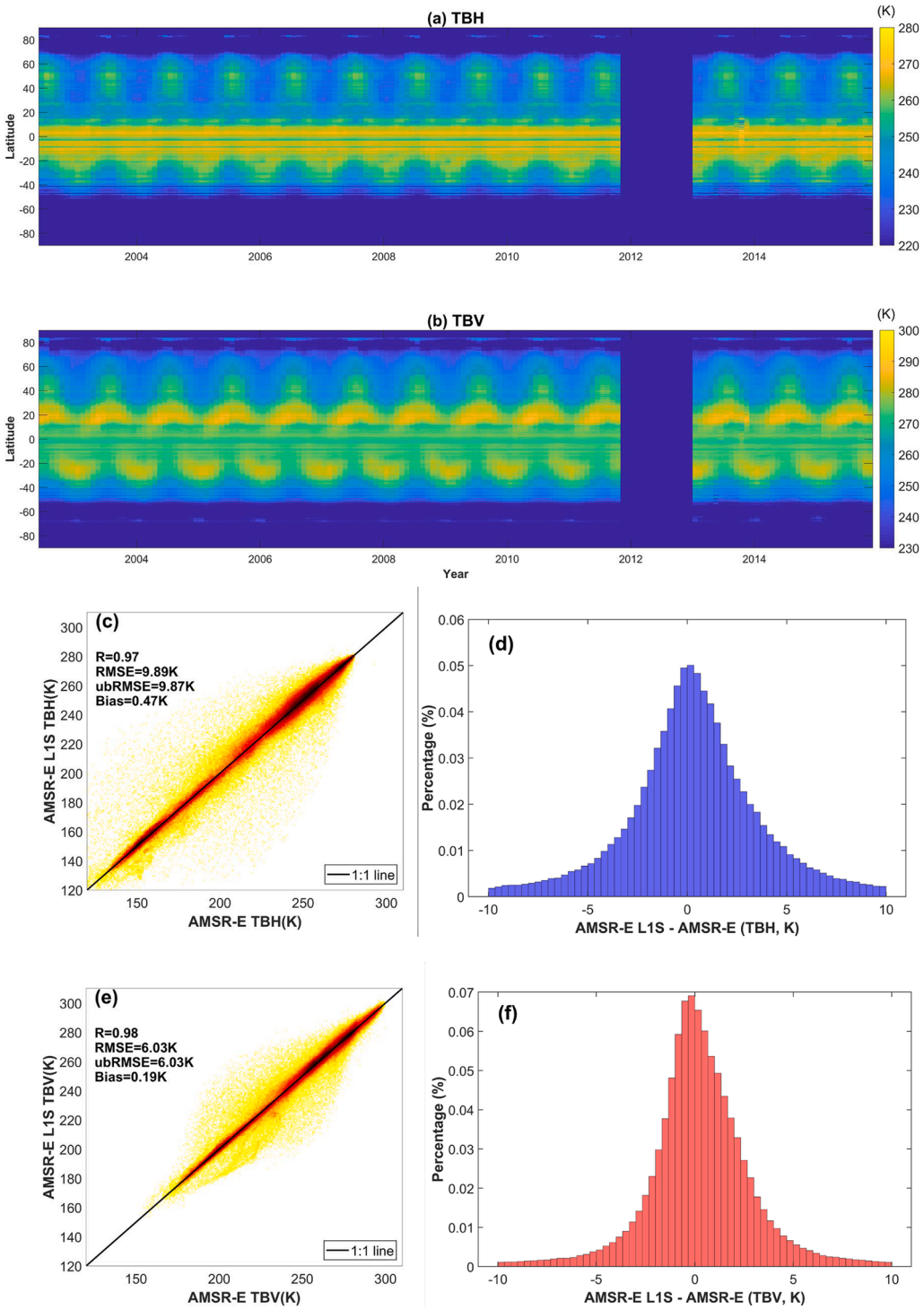

Fig. 4. Hovmöller diagrams showing the monthly mean values of TB per latitude for AMSR-E and AMSR-E L1S TB over they respective observation periods at H (a) and V (b) polarizations; Scatter plot of AMSR-E (September 2010 to August 2011) and AMSR-E L1S (April 2014 to March 2015) TB observations at H (c) and V (e) polarizations; Histogram of the difference between AMSR-E L1S and AMSR-E TB observations at H (d) and V (f) polarizations.

Table 2
Calibrated parameters for the global-based methods

Method	Polarization	Slope	Intercept	RMSE (K)
Method 1	H	0.98	8.76	5.35
Method 1	V	0.97	10.46	3.20
Method 2	H	0.98	7.91	3.95
Method 2	V	0.98	9.18	2.81

expecting that these spatial and temporal changes partly compensate each other at a large scale, leading to a low bias. It can be seen that the calibrated AMSR-E TB values computed with all the four methods are strongly correlated with the AMSR2 TB values both for the H and V polarizations ($R > 0.99$ at a global scale). However, results obtained from pixel-based methods (Method 3 and 4) appear to be slightly more scattered, as quantified by higher ubRMSE values ranging from 4.37 to 6.97 K compared with Method 1 and 2 which produced, respectively, a range of 3.12 to 3.57 K.

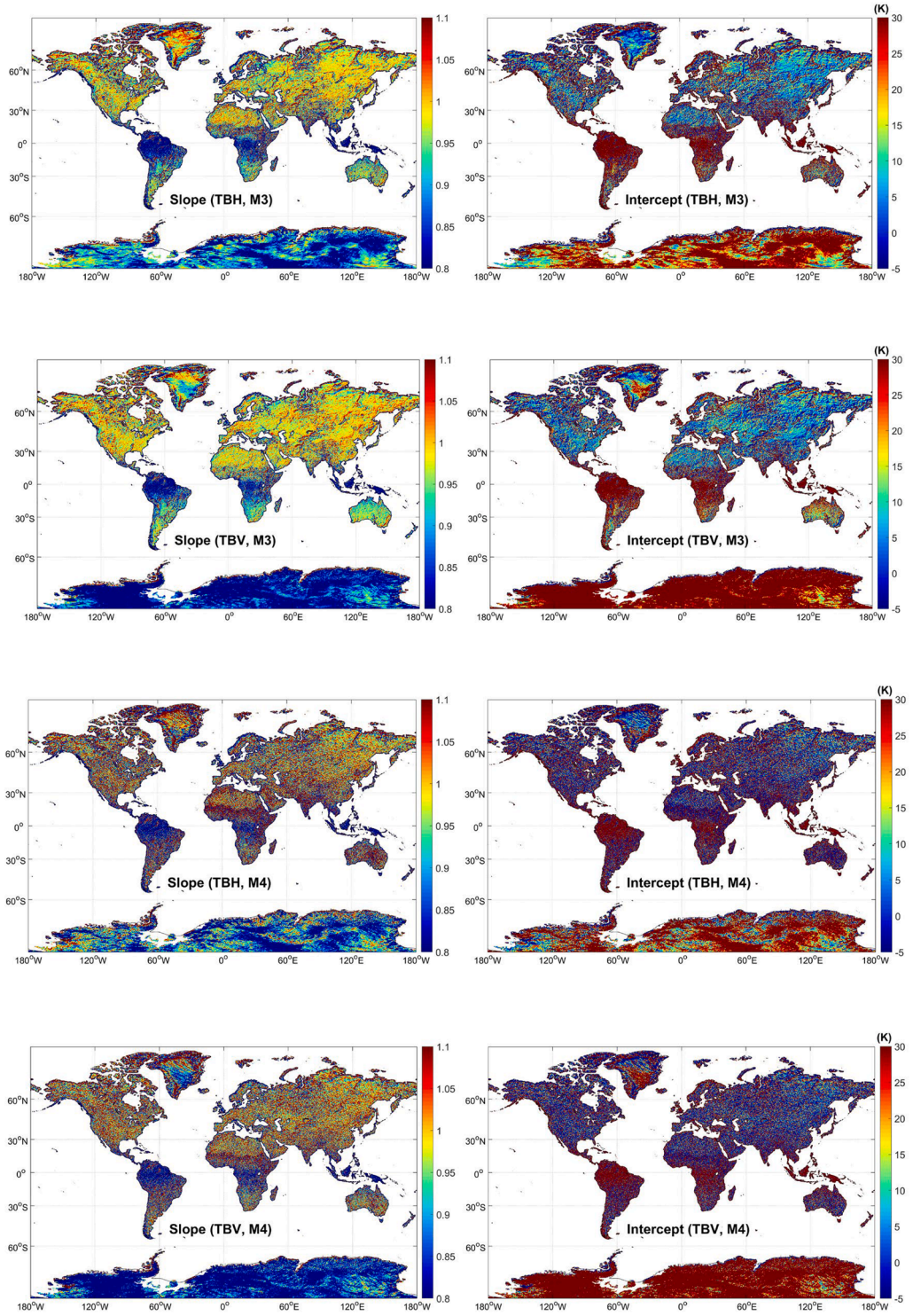

Fig. 5. Slope (1st row) and intercept (2nd row) maps at H (1st column) and V (2nd column) polarizations for Method 3, and at H (3rd column) and V (4th column) polarizations for Method 4.

As for EBF, mainly tropical forests, the results also show the advantages of using global-based methods rather than pixel-based methods by producing higher R and lower RMSE and ubRMSE values (Appendix Fig. 4). In addition, results obtained with Method 2 presented a lower bias of 0.14 and 0.03 K, respectively, for the H and V polarizations, compared with an underestimation of around 0.5 K for Method 1 (Fig. 7). Method 2 generally produced higher R values and lower RMSE, ubRMSE and bias (red colors) values than the three other methods. The result emphasized the interest of selecting homogeneous and temporally stable pixels to perform the calibration work.

3.3. Evaluation of X-VOD retrieved from the inter-calibrated TB data

The purpose of the TB calibration work described above was to merge the AMSRE and AMSR2 TB observations in order, in a second step, to produce a consistent long-term X-VOD product retrieved from the X-MEB model, spanning over the combined periods of observations of AMSR-E and AMSR2. In this section, we evaluated the consistency of

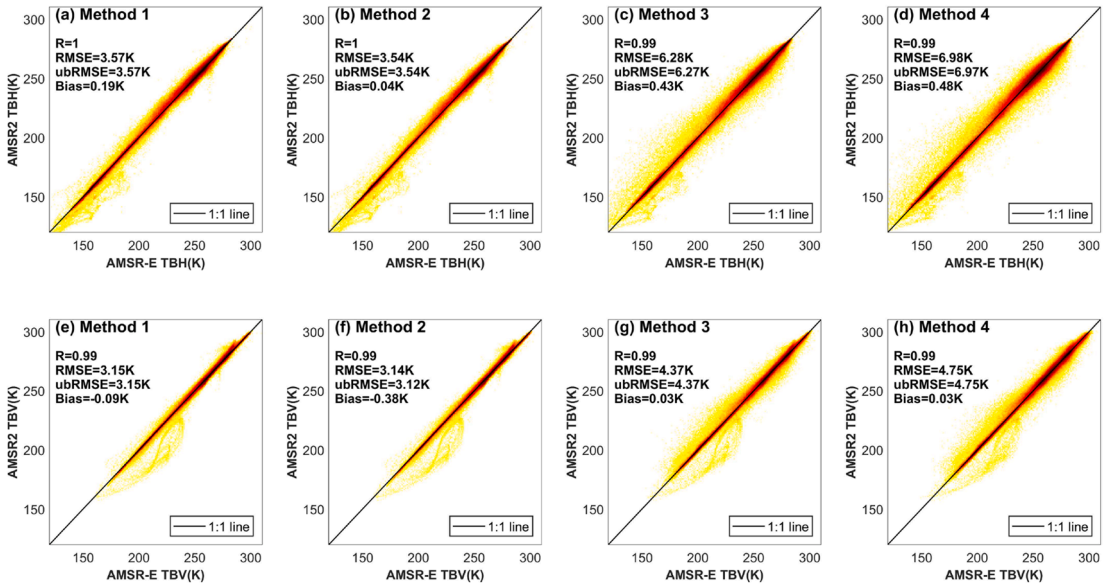

Fig. 6. Scatter plot of the calibrated AMSR-E TB (September 2010 to August 2011) by the four methods and AMSR2 TB (August 2012 to July 2013) at H (a, b, c, d) and V (e, f, g, h) polarizations.

	Method 1	Method 2	Method 3	Method 4
R (TBH, all landcover)	1	1	0.99	0.99
RMSE (TBH, all landcover), K	3.57	3.54	6.28	6.98
ubRMSE (TBH, all landcover), K	3.57	3.54	6.27	6.97
Bias (TBH, all landcover), K	0.19	0.04	0.43	0.48
R (TBV, all landcover)	0.99	0.99	0.99	0.99
RMSE (TBV, all landcover), K	3.15	3.14	4.37	4.75
ubRMSE (TBV, all landcover), K	3.15	3.12	4.37	4.75
abs(Bias (TBV, all landcover)), K	0.09	0.38	0.03	0.03
R (TBH, EBF)	0.99	0.99	0.97	0.95
RMSE (TBH, EBF), K	1.28	1.19	3.66	4.38
ubRMSE (TBH, EBF), K	1.16	1.18	3.61	4.33
Bias (TBH, EBF), K	0.53	0.14	0.59	0.71
R (TBV, EBF)	0.99	0.99	0.97	0.96
RMSE (TBV, EBF), K	0.77	0.64	1.91	2.2
ubRMSE (TBV, EBF), K	0.63	0.64	1.9	2.19
abs(Bias (TBV, EBF)), K	0.45	0.03	0.2	0.21

Fig. 7. Values of R, RMSE, ubRMSE and Bias between the calibrated AMSR-E and AMSR2 TB. Red > orange > yellow > light green > green > dark green represents the code of colours from the highest R, lowest RMSE, lowest ubRMSE and lowest Bias values to the lowest R, highest RMSE, highest ubRMSE and highest Bias values. (For interpretation of the references to color in this figure legend, the reader is referred to the web version of this article.)

X-VOD retrieved from the calibrated AMSR-E TB with the X-VOD index retrieved from AMSR2. This consistency was evaluated by analysing the relationships between X-VOD (obtained from both AMSR-E and AMSR2) with AGB/LAI/NDVI.

The consistency was evaluated for all the four AMSR-E TB merging methods (1 to 4) and for Original data (without calibration). Fig. 8 shows the evaluation results (in terms of R, RMSE, ubRMSE and absolute values of bias) obtained by evaluating X-VOD against the AGB (Bouvet and GlobBiomass), LAI and NDVI data sets. It can be seen that AMSR-E X-VOD is strongly correlated with AMSR2 X-VOD, with R values exceeding 0.98, no matter which calibration method was used. The main reason could be that the X-MEB inversion algorithm considered the initial VOD (VOD^{ini}) as a function of microwave polarization difference index (MPDI). It is likely that this step mitigated the effects of bias between the AMSRE and AMSR2 TB data as MPDI is less sensitive to the TB biases. Pixel-based methods (Method 3 and 4) led to worse performances than Methods 1 & 2, and even worse than considering the Original TB data. Method 2 outperformed all the other methods by producing higher

	Method 1	Method 2	Method 3	Method 4	Original TB
R(AMSR-E VOD, AMSR2 VOD)	0.994	0.995	0.990	0.988	0.993
RMSE(AMSR-E VOD, AMSR2 VOD)	0.037	0.036	0.049	0.055	0.045
ubRMSE(AMSR-E VOD, AMSR2 VOD)	0.037	0.036	0.049	0.055	0.042
abs(Bias(AMSR-E VOD, AMSR2 VOD))	0.001	0.002	0.002	0.003	0.015
R(AMSR-E VOD, Bouvet AGB)	0.906	0.907	0.871	0.862	0.903
R(AMSR2 VOD, Bouvet AGB)	0.902	0.902	0.902	0.902	0.902
R(AMSR-E VOD, GloBiomass)	0.936	0.936	0.905	0.897	0.931
R(AMSR2 VOD, GloBiomass)	0.933	0.933	0.933	0.933	0.933
R(AMSR-E VOD, LAI)	0.942	0.943	0.919	0.913	0.938
R(AMSR2 VOD, LAI)	0.942	0.942	0.942	0.942	0.942
R(AMSR-E VOD, NDVI)	0.971	0.971	0.958	0.955	0.971
R(AMSR2 VOD, NDVI)	0.971	0.971	0.971	0.971	0.971

Fig. 8. Evaluation result of the X-VOD products retrieved from the four methods and Original TB against AGB (Bouvet, GlobBiomass), LAI and NDVI. Red > orange > yellow > light green > green > dark green represents the code of colours from the highest R, lowest RMSE, lowest ubRMSE and lowest Bias values to the lowest R, highest RMSE, highest ubRMSE and highest Bias values. (For interpretation of the references to color in this figure legend, the reader is referred to the web version of this article.)

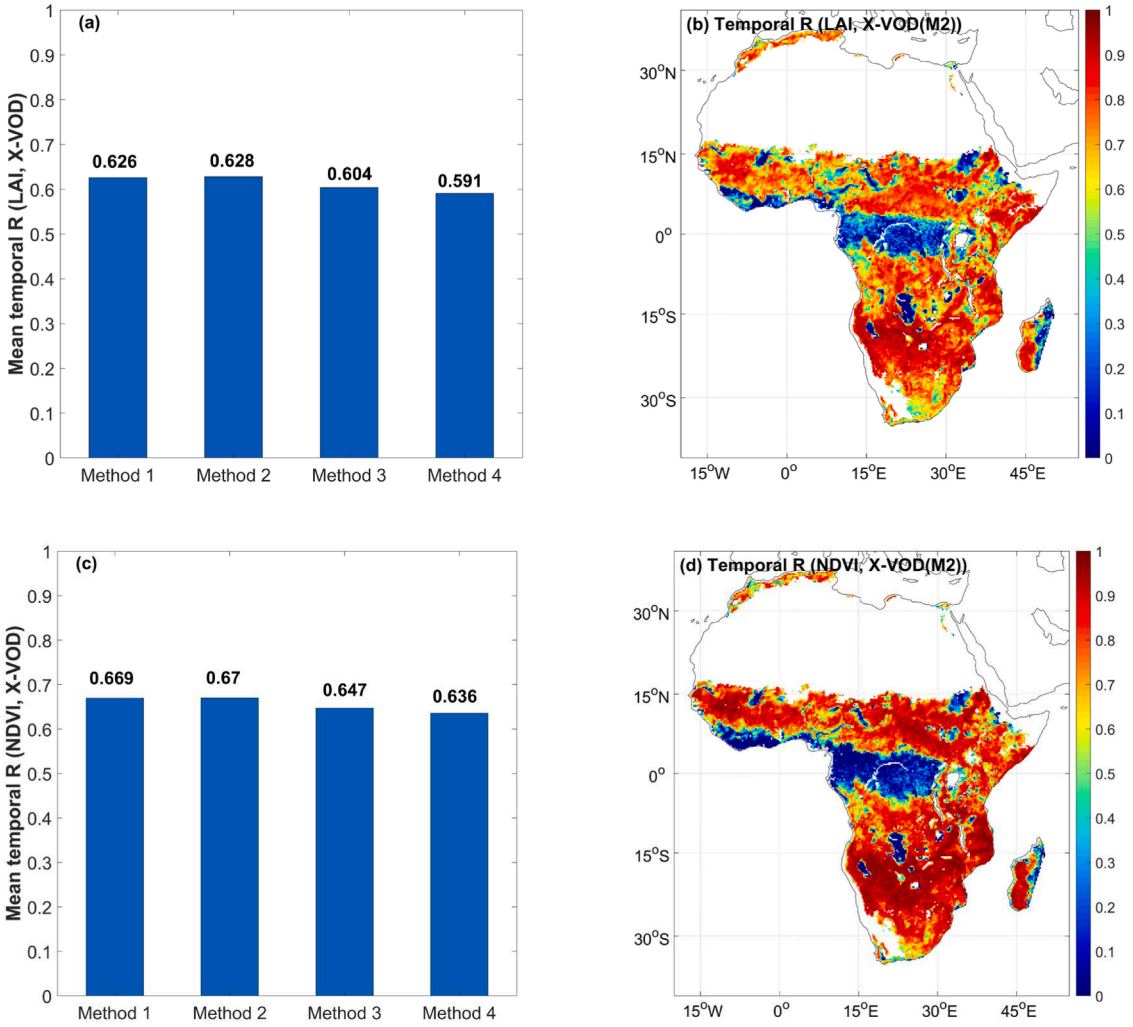

Fig. 9. Temporal correlation between LAI (a) and NDVI (c) and the combined X-VOD products over the combined AMSR-E (September 2010 to August 2011) and AMSR2 (August 2012 to July 2013) periods based on the four methods; The distribution of temporal correlation between LAI (b) and NDVI (d) and the combined X-VOD products based on Method 2.

R, lower RMSE and ubRMSE between the two X-VODs and by achieving higher spatial correlations with AGB, LAI and NDVI.

The results of the temporal consistency analysis are shown in Fig. 9. In each vegetated pixel, temporal correlation between LAI/NDVI and X-VOD was calculated (Fig. 9 (b, d) and Appendix Fig. 5), where X-VOD was computed from both the calibrated AMSR-E X-VOD (September 2010 to August 2011) and AMSR2 X-VOD (August 2012 to July 2013) products (used LAI/NDVI were from the corresponding two periods). Higher correlation was considered as corresponding to higher temporal consistency in the merging approach between the two periods. After averaging temporal correlation for all vegetated areas, we got histograms showing mean R for the four merging methods. Method 2 produced the highest scores with mean temporal correlations reaching 0.628 and 0.67, respectively with LAI and NDVI, then closely followed by Method 1. In comparison, pixel-based methods (Method 3 & 4) showed lower performances. It can be seen from the temporal correlation distributions that stronger correlations were mainly located in sparse vegetation while weaker correlations were found in dense vegetation areas (where temporal changes in X-VOD are much lower).

To be more specific, we illustrated in Fig. 10, the time variations of the five X-VOD products (Method 1, 2, 3, 4 and Original data) over a few randomly selected pixels with different land covers (GRA, EBF, SAV) and in different countries (Sudan, Cameroon and Central African Republic). These pixels had similar vegetation and soil moisture conditions over the selected AMSR-E and AMSR2 periods, so that they can be used to assess the performances of different methods. We generally found that the values of the different AMSR-E X-VOD products increased or decreased coherently. Method 2 generally produced more consistent AMSR-E X-VOD (including more consistent high and low values) with AMSR2 X-VOD. For pixels shown in Fig. 10(b) and (c), X-VOD retrieved from the Original TB data was underestimated, to some extent, compared with AMSR2 X-VOD. The calibrated results corrected the underestimation, but with a small over-correction for Method 3 and 4. The results illustrate the advantage of using Method 1 and 2 for merging the AMSR-E and AMSR2 TB data in order to retrieve X-VOD. More results with pixels including X-VOD, LAI and soil moisture time series are shown in Appendix Fig. 6.

3.4. Comparison of AMSR-E X-VOD by Method 2 with AMSR2 X-VOD

Based on the evaluation results presented above, Method 2 provided the best performance by producing highest R, lowest RMSE and ubRMSE values between AMSR-E X-VOD and AMSR2 X-VOD and by achieving highest spatial correlations with AGB, LAI and NDVI. Therefore, we focus on Method 2 in the following analyses. Fig. 11(a) shows the spatial distribution of yearly averaged X-VOD retrieved from the Method-2-calibrated AMSR-E observations over the last running year of its period from September 2010 to August 2011. Generally, the X-VOD values in Africa ranged from 0 to 1.1, and presented a decreasing trend from the equator to higher-latitude regions. High values were mainly located in tropical forests (≈1.0), while low values were distributed near the Sahara Desert and the southwest coastline of Africa. Looking at the distribution of the X-VOD bias between AMSR2 (over the first running year) and AMSR-E (Fig. 11b), we can see large regions of Africa (green areas) were covered by subtle differences. High correlation values, low RMSE, ubRMSE and bias values between AMSR-E and AMSR2 X-VOD can be noted in Fig. 11(c). On the other hand, clear bias values could be noted in a few regions: positive values in Ethiopia and negative values mainly in the South of Africa. More specifically, the X-VOD differences varied significantly among different vegetation types. It can be seen from Fig. 11(d) that EBF, DBF, WSA, SAV, GRA, CRO and BAR classes shared a very low bias (lower than 0.01) compared with CSH and CVM that both presented a clear positive bias (>0.02) and OSH with a clear negative bias (≈ −0.03). Even though the selected periods are close in time, there still is a gap of 11 months. So, the X-VOD difference over sparse-vegetated areas may be caused by vegetation growth/degradation or changes in vegetation water content.

The relationships between X-VOD and AGB/LAI/NDVI are quite

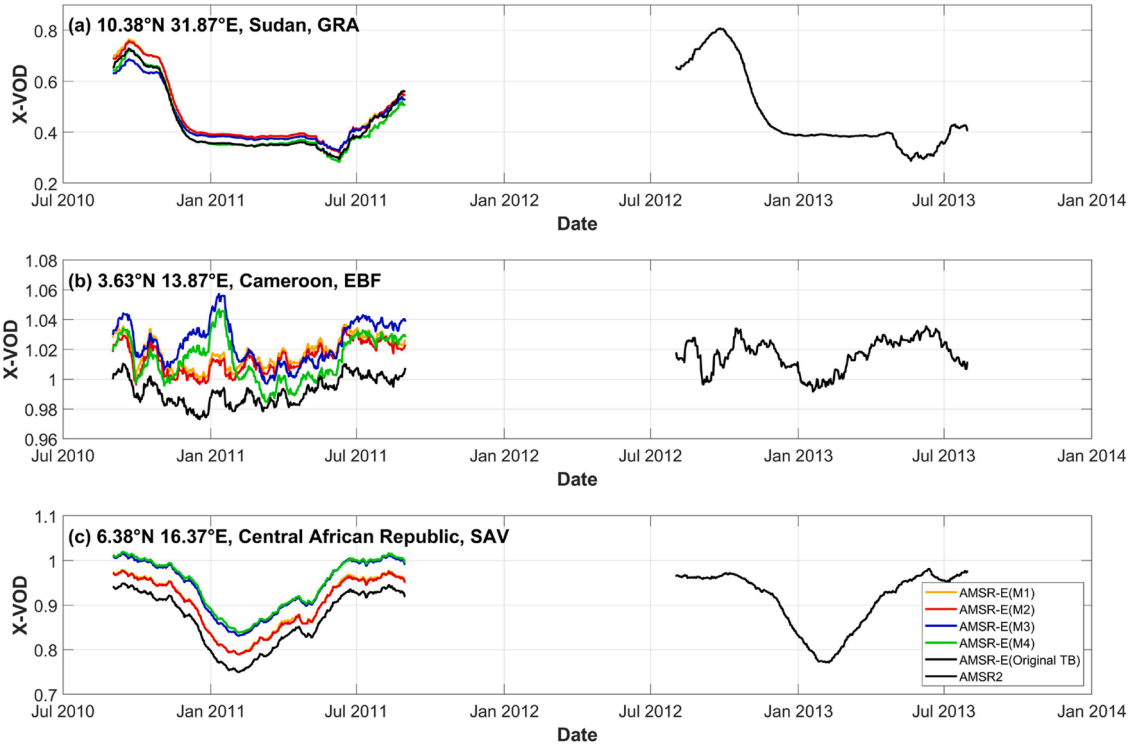

Fig. 10. Time series of AMSR-E X-VOD for five different methods (yellow: Method 1, red: Method 2, blue: Method 3, green: Method 4, black: Original TB) and AMSR2 X-VOD for one pixel over Grasslands (GRA) (a), Evergreen Broadleaf Forests (EBF) pixel (b) and Savanna (SAV) (c). (For interpretation of the references to color in this figure legend, the reader is referred to the web version of this article.)

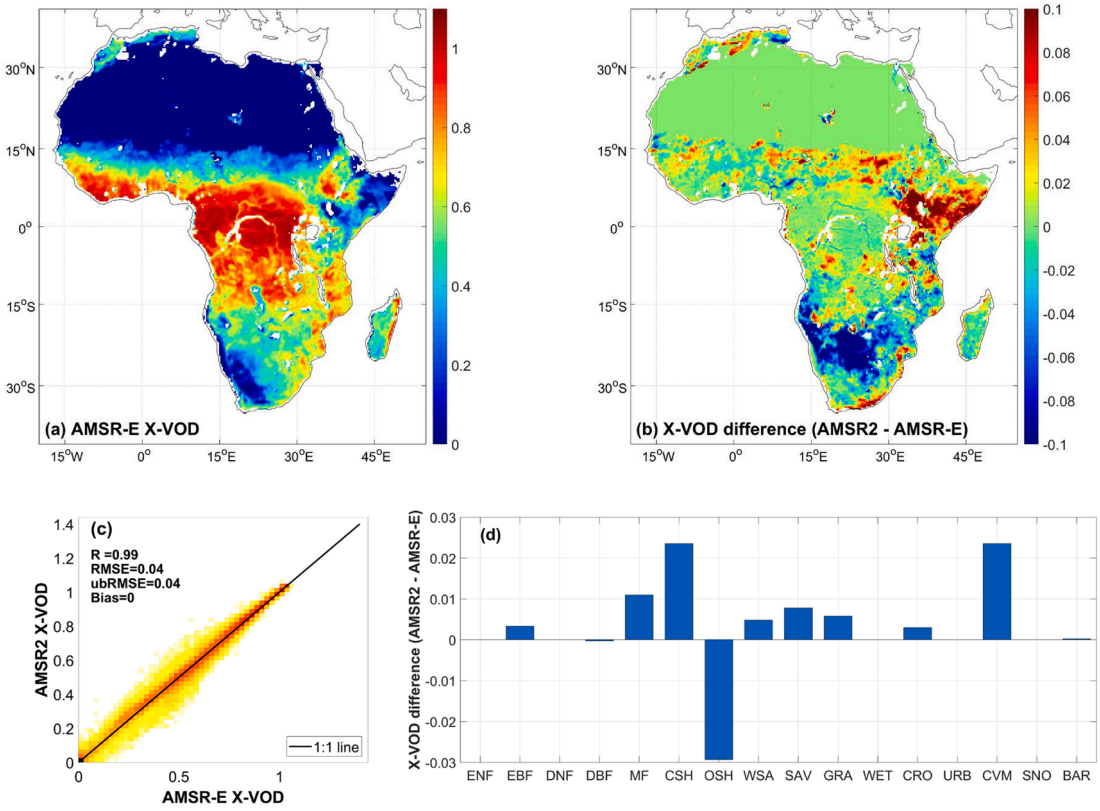

Fig. 11. Spatial distribution of (a) X-VOD over the last running year of AMSR-E (September 2010 to August 2011) and (b) the difference between AMSR-E X-VOD and AMSR2 X-VOD for the first running year (August 2012 to July 2013); (c) Scatter plot of AMSR-E and AMSR2 X-VOD; (d) Histogram of the difference between AMSR-E X-VOD and AMSR2 X-VOD for each vegetation class. There are less than 30 pixels or even no pixels for ENF, DNF, WET, URB and SNO classes in Africa, so there is no X-VOD bias value for these classes.

consistent after calibration for AMSR-E and AMSR2 over their respective periods (AMSR-E: September 2010 to August 2011; AMSR2: August 2012 to July 2013). The Bouvet and GlobBiomass AGB and LAI exponentially connect with IB X-VOD, while NDVI shows a good linear relationship (Fig. 12). The fitted lines (black) for AMSR-E X-VOD (Method 2) are closer to the fitted lines (blue) for AMSR2 X-VOD than the fitted lines (green) for AMSR-E X-VOD (Original TB). This result indicates that the merging method 2 has reduced the discrepancy of AMSR-E (based on Original TB data) and AMSR2 X-VOD. In addition, AMSR-E X-VOD had almost the same correlation values as AMSR2 X-VOD when it is compared to AGB, LAI, NDVI. The two fitted lines (black and blue) appear as almost totally overlapped in all plots which confirms the consistency of the calibrated functions between X-VOD and AGB/LAI/NDVI, whether considering AMSR-E X-VOD (calibrated with

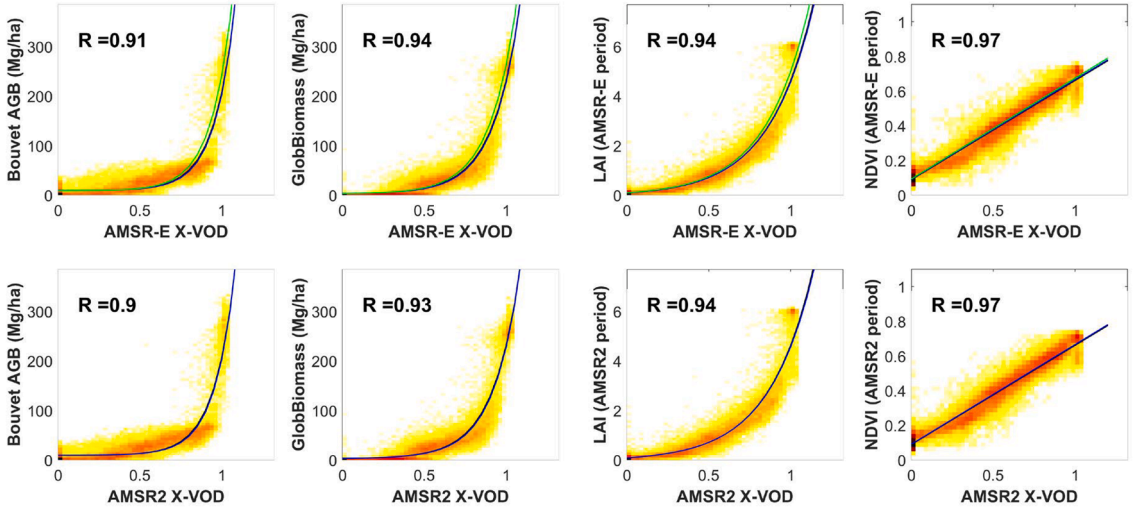

Fig. 12. Scatter plot between X-VOD retrieved from AMSR-E TB (calibrated based on Method 2) and AMSR2 TB and Bouvet and GlobBiomass AGB, LAI, NDVI. Green lines are the fitted lines between AMSR-E X-VOD (based on the original TB) and AGB/LAI/NDVI; Black lines are the fitted lines between AMSR-E X-VOD (Method 2) and AGB/LAI/NDVI; Blue lines are the fitted lines between AMSR2 X-VOD and AGB/LAI/NDVI. (For interpretation of the references to color in this figure legend, the reader is referred to the web version of this article.)

Method 2) or AMSR2 X-VOD.

IB X-VOD was extended to the whole period of AMSR-E (June 2002 - October 2011) and AMSR2 (July 2012 - present) observations. Fig. 13 illustrates the merged IB X-VOD (based on Method 2) over almost 20 years in the whole Africa and in each IGBP class. It can be seen that IB X-VOD shows a high temporal consistency over the combined AMSR-E and AMSR2 periods after the calibration work. Even though the changes in the averaged X-VOD in the whole Africa are not equivalent to carbon stock changes as AGB is exponentially linked with X-VOD, some vegetation losses and gains are shown in the X-VOD time series. X-VOD decreases in 2003, 2011, 2015–2016 and increases in 2008–2009, 2017, in agreement with previous vegetation carbon stock studies (Liu et al., 2015; Fan et al., 2019; Wigneron et al., 2020). More attention in our further work will be put on the dynamics of AGB (based on IB X-VOD) in Africa from 2002 to the present.

4. Discussion

In this study, four different methods were applied to merge the AMSR-E and AMSR2 TB observations, two of which are on a global basis (Method 1 & 2) and the two others are on a pixel basis (Method 3 & 4). We evaluated the effectiveness of the four methods by comparing directly the calibrated AMSR-E TB with AMSR2 TB, and also by evaluating the retrieved X-VOD against AGB/LAI/NDVI. The results suggest that pixel-based methods provided lower performance than global-based methods and even than the Original TB method (*i.e.* with no calibration of the AMSR-E TB data). Pixel-based methods slightly over-corrected the X-VOD values for some pixels (Fig. 10). This could be related to the fact that the pixel-based methods were based on a very limited number of observations (around or less than 40 overpasses in some areas (Fig. 14)), due to the slower rotation of AMSR-E L1S. Similar issues, namely insufficient overlapping observations, also exist in prior studies. For example, Du et al. (2014) used an inverse distance weighting method for spatial interpolation estimation of the slope and intercept from nearby pixels. But the function built in nearby pixels may not be suitable for the target pixel because of the heterogeneity in the land surface conditions. Moesinger et al. (2020) directly used observations of the last two years of AMSR-E and the first two years of AMSR2 to determine the scaling parameters which removed any potential trends in the combined periods and the gap period. The authors of this study chose global-based methods because it allows the use of a large number of observations as the training data.

Method 2, based on homogeneous and temporally stable pixels (EBF and SNO) to build the calibration functions led to improved accuracy in comparison to Method 1, which considers all non-water pixels. This may result from the fact Method 2 is less sensitive to changing environmental conditions (in soil moisture and vegetation) between the two periods used to calibrate the merging function; these changing conditions affecting more the low vegetation pixels used in Method 1. Meier and Ivanoff (2017) displayed the regression coefficients (slope and intercept) of the 18, 36 and 89 GHz channels for different months which are very close to each other, but still show slight differences. In this study, choosing observations over the EBF and SNO classes (which keep more stable over the full year (Fig. 2)) as the training data sets to do the TB calibration avoids to be sensitive to seasonal vegetation effects over low vegetation classes.

Even though Method 2, which produced the best performances, was chosen in this study, the uncertainty in the calibration method could come from that i) the calibrated global-based function does not account for the different vegetation structures of the various land cover classes; ii) the calibrated time-independent function may vary over different seasons due to the variable climate and environment even though the selected method presented mitigated seasonal variations. For instance, as shown in Fig. 15, the functions (slope and intercept) based on Method 2 indicate a generally stable but locally fluctuating tendency over different months. On the other hand, the fact that the selected method (Method 2) is not a season- or IGBP-based method is an advantage, as it made the method more simple and robust.

In this study, two optical vegetation variables (LAI and NDVI) were used to evaluate the consistency of X-VOD obtained from both the calibrated-AMSR-E and AMSR2 TB data. However, the greenness changes in vegetation detected by the optical techniques may be asynchronous with the microwave-based vegetation features (VOD). For example, the vegetation indices retrieved from optical observations can be affected by the sun-sensor geometry (Morton et al., 2014). In addition, there may be time lags between the optical-based leaf phenology and the microwave-based plant water storage, especially in dense vegetation (Tian et al., 2018). Introducing a third index (LAI/NDVI) to calculate the temporal correlation with the combined AMSR-E and AMSR2 X-VOD can help to assess the temporal consistency of the

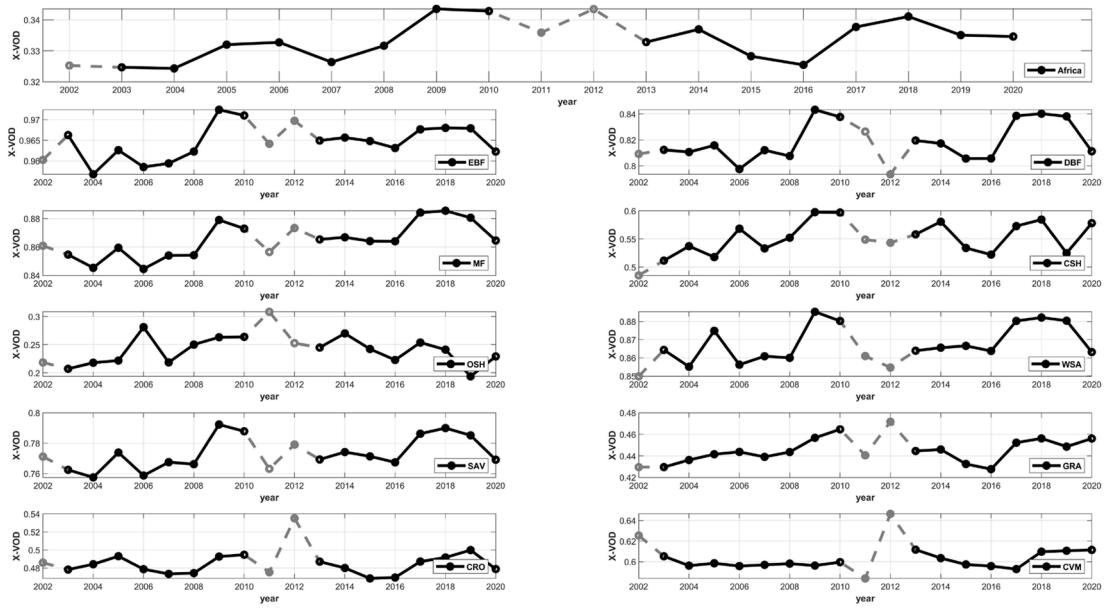

Fig. 13. IB X-VOD over the AMSR-E and AMSR2 periods. Black lines and dots mean data in the whole year are available, while year 2001, 2011 and 2012 are marked in grey color because they are the years when AMSR-E/AMSR2 started or terminated and data in some months are unavailable.

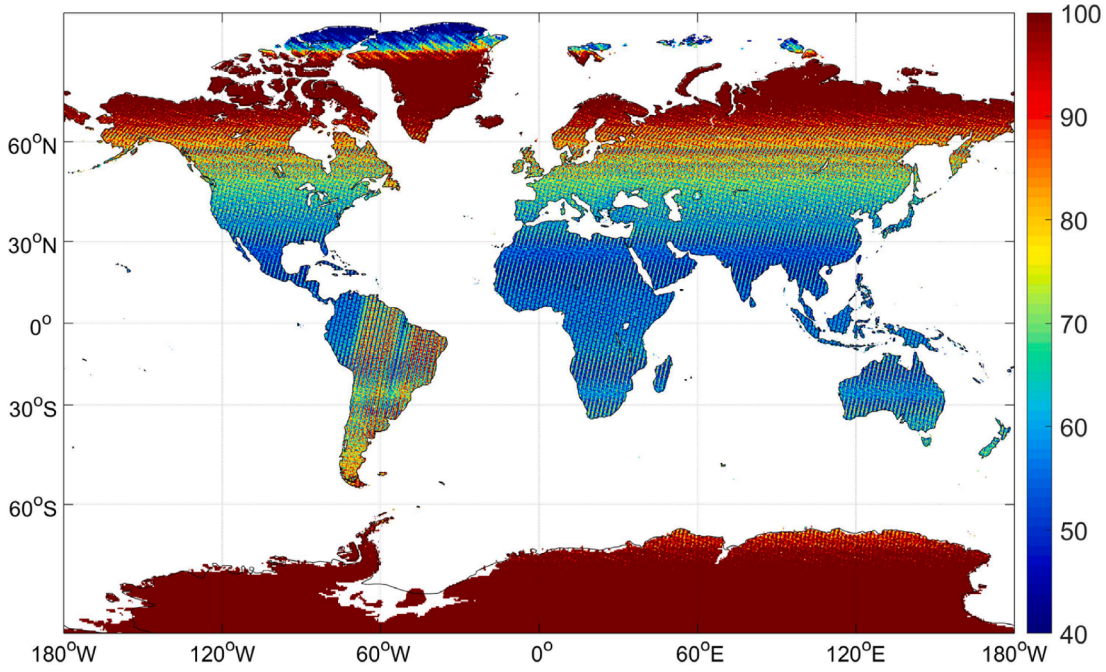

Fig. 14. The global distribution of the number of available AMSR-E L1S observations from December 2012 to December 2015.

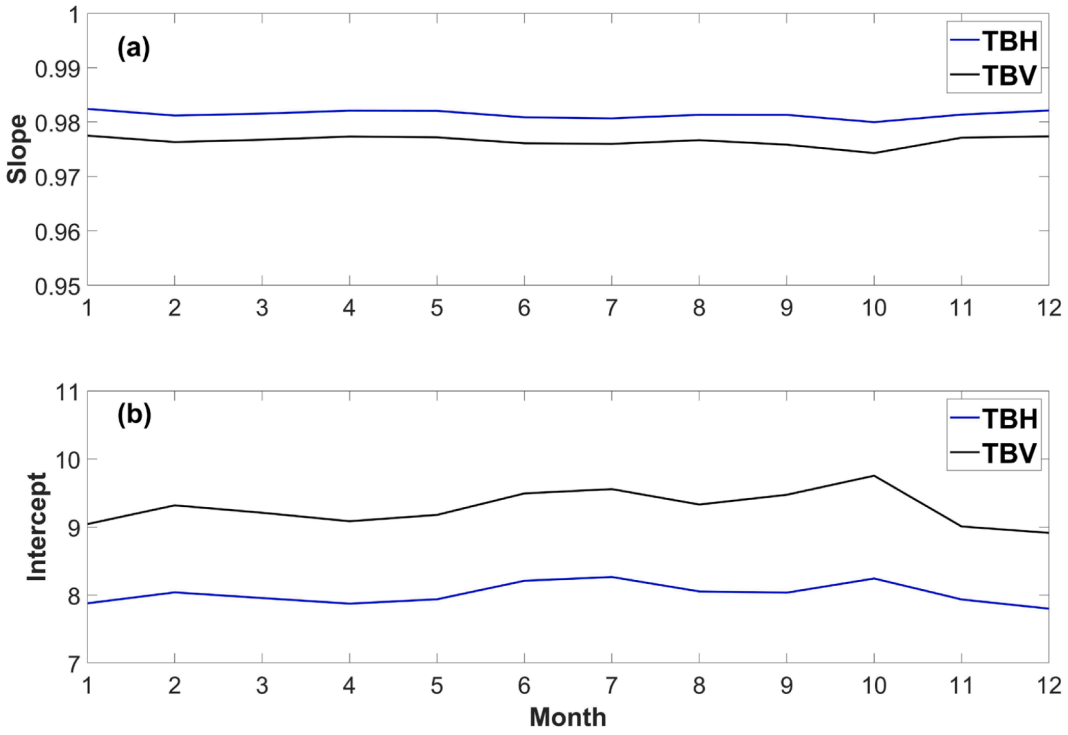

Fig. 15. Monthly global regression coefficients (a: Slope, b: Intercept) fitting AMSR-E L1S to AMSR2 observations.

merged X-VOD in considering the real vegetation growth and degradation. It should be also noted that the errors associated with the LAI/NDVI indices may introduce uncertainty in the evaluation step.

5. Conclusion

The aims of the present study were to evaluate the use of four different approaches in merging brightness temperature observations from both the AMSR-E and AMSR2 sensors, and then to retrieve a consistent X-VOD product. The evaluation considered both (i) the comparison results between the calibrated AMSR-E TB and AMSR2 TB and (ii) the evaluation results of the X-VOD data sets retrieved from those two TB data sets against AGB (Bouvet and GlobBiomass)/ LAI/ NDVI. Both evaluations (i) and (ii) suggest that Method 2, which built a global-based calibration function based on homogeneous and temporally stable land covers (EBF and SNO), showed distinct advantages over the other methods. In addition, the fitted relationships between X-VOD and AGB/LAI/NDVI match very well over the AMSR-E and AMSR2

periods after the calibration work, making us confident in the possibility of producing a consistent X-VOD product over a long period. Note, more generally the specific method developed in this study to merge observations from different sensors can be extended to other satellite datasets or products.

Future works will consider: i) to extend IB X-VOD to the whole observation periods of AMSR-E (June 2002 - September 2011) and AMSR2 (July 2012 - present), and then to analyse the dynamics of X-VOD (as a proxy of AGB) in Africa over the whole period (2002-present) of almost 20 years; ii) to extend the X-MEB model to the global scale, paying particular attention to the RFI effect particularly in Europe (Lacava et al., 2012). The validation of the merging Method 2, evaluated here only over Africa, will also be extended to the global scale; iii) to retrieve VOD at C-band (C-VOD) and examine the different sensitivities of C- and X-VOD to vegetation.

CRediT authorship contribution statement

Mengjia Wang: Conceptualization, Methodology, Investigation, Data curation, Writing – original draft. **Jean-Pierre Wigneron:** Conceptualization, Methodology, Writing – review & editing, Supervision, Funding acquisition. **Rui Sun:** Writing – review & editing, Funding acquisition. **Lei Fan:** Writing – review & editing. **Frédéric Frappart:** Writing – review & editing. **Shengli Tao:** Writing – review & editing. **Linna Chai:** Writing – review & editing. **Xiaojun Li:** Writing – review & editing. **Xiangzhuo Liu:** Writing – review & editing. **Hongliang Ma:** Writing – review & editing. **Christophe Moisy:** Writing – review & editing. **Philippe Ciais:** Writing – review & editing.

Declaration of Competing Interest

The authors declare that they have no known competing financial interests or personal relationships that could have appeared to influence the work reported in this paper.

Acknowledgements

This work was jointly supported CNES-TOSCA (Centre National d'Etudes Spatiales, France) and by the National Natural Science Foundation of China (41471349) funding and Mengjia WANG was sponsored by China Scholarship Council (CSC; 201906040124).

Appendix A. Supplementary material

Supplementary data to this article can be found online at https://doi.org/10.1016/j.jag.2021.102609.

References

Bastos, A., et al., 2018. Impact of the 2015/2016 El Nino on the terrestrial carbon cycle constrained by bottom-up and top-down approaches. Philos. Trans. R. Soc. Lond. B Biol. Sci. 373.
Baur, M.J., et al., 2019. Estimation of relative canopy absorption and scattering at L-, C- and X-bands. Remote Sensing of Environment 233.
Beck, H.E., et al., 2020. Evaluation of 18 satellite- and model-based soil moisture products using in situ measurements from 826 sensors. Earth Syst. Sci. Discussion.
Bhatt, R., et al., 2014. Initial Stability Assessment of S-NPP VIIRS Reflective Solar Band Calibration Using Invariant Desert and Deep Convective Cloud Targets. Remote Sens. 6, 2809–2826.
Bouvet, A., et al., 2018. An above-ground biomass map of African savannahs and woodlands at 25 m resolution derived from ALOS PALSAR. Remote Sens. Environ. 206, 156–173.
Brandt, M., et al., 2018. Satellite passive microwaves reveal recent climate-induced carbon losses in African drylands. Nat. Ecol. Evol. 2, 827–835.
Chen, J., et al., 2017. Remote estimation of colored dissolved organic matter and chlorophyll-a in Lake Huron using Sentinel-2 measurements. J. Appl. Remote Sens. 11.
Das, N.N., et al., 2014. Intercomparisons of Brightness Temperature Observations Over Land From AMSR-E and WindSat. IEEE Trans. Geosci. Remote Sens. 52, 452–464.
de Nijs, A.H.A., et al., 2015. A Methodology to Determine Radio-Frequency Interference in AMSR2 Observations. IEEE Trans. Geosci. Remote Sens. 53, 5148–5159.
Du, J., et al., 2014. Inter-Calibration of Satellite Passive Microwave Land Observations from AMSR-E and AMSR2 Using Overlapping FY3B-MWRI Sensor Measurements. Remote Sens. 6, 8594–8616.
Du, J., et al., 2015. Passive Microwave Remote Sensing of Soil Moisture Based on Dynamic Vegetation Scattering Properties for AMSR-E. IEEE Trans. Geosci. Remote Sens. 54, 597–608.
Du, J., et al., 2017. A global satellite environmental data record derived from AMSR-E and AMSR2 microwave Earth observations. Earth Syst. Sci. Data 9, 791–808.
Duveiller, G., et al., 2018. The mark of vegetation change on Earth's surface energy balance. Nat. Commun. 9, 1–12.
Fan, L., et al., 2019. Satellite-observed pantropical carbon dynamics. Nat. Plants 5, 944–951.
Fang, G.H., et al., 2015. Comparing bias correction methods in downscaling meteorological variables for a hydrologic impact study in an arid area in China. Hydrol. Earth Syst. Sci. 19, 2547–2559.
Feldman, A.F., et al., 2018. Moisture pulse-reserve in the soil-plant continuum observed across biomes. Nat. Plants 4, 1026–1033.
Frappart, F., et al., 2020. Global Monitoring of the Vegetation Dynamics from the Vegetation Optical Depth (VOD): A Review. Remote Sens. 12.
Haerter, J.O., et al., 2011. Climate model bias correction and the role of timescales. Hydrol. Earth Syst. Sci. 15, 1065–1079.
Hu, T., et al., 2019. A continuous global record of near-surface soil freeze/thaw status from AMSR-E and AMSR2 data. Int. J. Remote Sens. 40, 6993–7016.
Imaoka, K., et al., 2010. Global Change Observation Mission (GCOM) for Monitoring Carbon, Water Cycles, and Climate Change. Proc. IEEE 98, 717–734.
Imaoka, K., et al., 2016. Characteristics of AMSR-E slow rotation data. IEEE International Geoscience and Remote Sensing Symposium (IGARSS), 883-885.
JAXA, 2009. AMSR-E Data Users Handbook.
JAXA, 2016. Data users' manual for the advanced microwave scanning radiometer 2 (AMSR2) onboard the global change observation mission 1st—water "SHIZUKU"(GCOM-W1).
Jones, M.O., et al., 2012. Satellite passive microwave detection of North America start of season. Remote Sens. Environ. 123, 324–333.
Kawanishi, T., et al., 2003. The advanced microwave scanning radiometer for the earth observing system (AMSR-E), NASDA's contribution to the EOS for global energy and water cycle studies. IEEE Trans. Geosci. Remote Sens. 41, 184–194.
Kolassa, J., et al., 2016. Soil moisture retrieval from AMSR-E and ASCAT microwave observation synergy. Part 1: Satellite data analysis. Remote Sens. Environ. 173, 1–14.
Konings, A.G., Gentine, P., 2017. Global variations in ecosystem-scale isohydricity. Glob Chang Biol 23, 891–905.
Kumar, S.V., et al., 2020. Assimilation of vegetation optical depth retrievals from passive microwave radiometry. Hydrol. Earth Syst. Sci. 24, 3431–3450.
Lacava, T., et al., 2012. A comprehensive analysis of AMSRE C- and X-bands Radio Frequency Interferences.
Li, M., et al., 2020. Comprehensive evaluation of soil moisture and soil temperature from third-generation atmospheric and land reanalysis datasets. Int. J. Climatol.
Li, X., et al., 2021. Global-scale assessment and inter-comparison of recently developed/reprocessed microwave satellite vegetation optical depth products. Remote Sens. Environ. 253.
Liu, Y.Y., et al., 2011. Global long-term passive microwave satellite-based retrievals of vegetation optical depth. Geophys. Res. Lett. 38, n/a-n/a.
Liu, Y.Y., et al., 2015. Recent reversal in loss of global terrestrial biomass. Nat. Clim. Change 5, 470–474.
Ma, H., et al., 2021. Evaluation of six satellite- and model-based surface soil temperature datasets using global ground-based observations. Remote Sens. Environ. 264.
Meier, W.N., Ivanoff, A., 2017. Intercalibration of AMSR2 NASA Team 2 Algorithm Sea Ice Concentrations With AMSR-E Slow Rotation Data. IEEE J. Sel. Top. Appl. Earth Obs. Remote Sens. 10, 3923–3933.
Mermoz, S., et al., 2015. Decrease of L-band SAR backscatter with biomass of dense forests. Remote Sens. Environ. 159, 307–317.
Mo, T., et al., 1982. A model for microwave emission from vegetation-covered fields. J. Geophys. Res. 87.
Moesinger, L., et al., 2020. The global long-term microwave Vegetation Optical Depth Climate Archive (VODCA). Earth Syst. Sci. Data 12, 177–196.
Morton, D.C., et al., 2014. Amazon forests maintain consistent canopy structure and greenness during the dry season. Nature 506, 221–224.
Owe, M., et al., 2008. Multisensor historical climatology of satellite-derived global land surface moisture. J. Geophys. Res. 113.
Owe, M., et al., 2001. A Methodology for Surface Soil Moisture and Vegetation Optical Depth Retrieval Using the Microwave Polarization Difference Index. IEEE Trans. Geosci. Remote Sens. 39.
Prigent, C., et al., 2007. Global inundation dynamics inferred from multiple satellite observations, 1993–2000. J. Geophys. Res. 112.
Qin, Y., et al., 2021. Carbon loss from forest degradation exceeds that from deforestation in the Brazilian Amazon. Nat. Clim. Change 11, 442–448.
Rodríguez-Fernández, N.J., et al., 2018. An evaluation of SMOS L-band vegetation optical depth (L-VOD) data sets: high sensitivity of L-VOD to above-ground biomass in Africa. Biogeosciences 15, 4627–4645.
Rozendaal, D.M.A., et al., 2017. DUE GlobBiomass D17 Validation Report.
Shimada, M., 2011. Model-based polarimetric SAR calibration method using forest and surface-scattering targets. IEEE Trans. Geosci. Remote Sens. 49, 1712–1733.
Shimoda, H., et al., 2012. Status of AMSR2 instrument on GCOM-W1. Earth Observing Missions and Sensors: Development, Implementation, and Characterization II.
Swinnen, E., Toté, J.D.-N.G.A.N.k.-V., 2017. Gio Global Land Component–Lot I "Operation of the Global Land Component", Framework Service Contract N 388533

(JRC), Algorithm Theoretical Basis Document, Normalized Difference Vegetation Index (NDVI), Collection 1km, Version 2.2. 21.
Tian, F., et al., 2016. Remote sensing of vegetation dynamics in drylands: Evaluating vegetation optical depth (VOD) using AVHRR NDVI and in situ green biomass data over West African Sahel. Remote Sens. Environ. 177, 265–276.
Tian, F., et al., 2018. Coupling of ecosystem-scale plant water storage and leaf phenology observed by satellite. Nat. Ecol. Evol. 2, 1428–1435.
Tong, X., et al., 2020. Forest management in southern China generates short term extensive carbon sequestration. Nat. Commun. 11, 129.
Wang, M., et al., 2021. An alternative AMSR2 vegetation optical depth for monitoring vegetation at large scales. Remote Sens. Environ. 263.
Wang, M., et al., 2020. Evaluation and Comparison of Light Use Efficiency and Gross Primary Productivity Using Three Different Approaches. Remote Sens. 12.
Wigneron, J.-P., et al., 1995. A Simple Algorithm to Retrieve Soil Moisture and Vegetation Biomass Using Passive Microwave Measurements over Crop Fields. Remote Sens. Environ. 51, 331–341.
Wigneron, J.-P., et al., 2008. Estimating the Effective Soil Temperature at L-Band as a Function of Soil Properties. IEEE Trans. Geosci. Remote Sens. 46, 797–807.
Wigneron, J.-P., et al., 2007a. Estimation of microwave parameters of crops from radiometric measurements. Int. J. Remote Sens. 17, 2875–2880.
Wigneron, J.-P., et al., 2020. Tropical forests did not recover from the strong 2015–2016 El Niño event. Science. Advances 6.
Wigneron, J.-P., et al., 2017. Modelling the passive microwave signature from land surfaces: A review of recent results and application to the L-band SMOS & SMAP soil moisture retrieval algorithms. Remote Sens. Environ. 192, 238–262.
Wigneron, J.-P., et al., 2007b. L-band Microwave Emission of the Biosphere (L-MEB) Model: Description and calibration against experimental data sets over crop fields. Remote Sens. Environ. 107, 639–655.
Wigneron, J.-P., et al., 2021. SMOS-IC data record of soil moisture and L-VOD: Historical development, applications and perspectives. Remote Sens. Environ. 254, 112238.
Willmott, C.J., 1981. On the validation of models. Phys. Geogr. 2, 184–194.
Wu, B., et al., 2020. A Fundamental Climate Data Record Derived from AMSR-E, MWRI, and AMSR2. IEEE Trans. Geosci. Remote Sens. 58, 5450–5461.
Yao, P., et al., 2021. A long term global daily soil moisture dataset derived from AMSR-E and AMSR2 (2002–2019). Sci. Data 8 (143). https://doi.org/10.1038/s41597-021-00925-8.
Yu, T., et al., 2021. Comparison of Machine Learning Methods to Up-Scale Gross Primary Production. Remote Sensing 13.
Zhang, Q., et al., 2021. Generating seamless global daily AMSR2 soil moisture (SGD-SM) long-term products for the years 2013–2019. Earth Syst. Sci. Data 13, 1385–1401.